RESEARCH ARTICLE

Key Points:
- Two high-resolution seismic reflection profiles were acquired 30 km upstream of the calving front at the center flow line of Store Glacier, a fast-flowing tidewater glacier draining the western sector of the Greenland ice sheet
- Analysis reveals an 80 m thick layer of anisotropic, horizontally easily deformable basal ice, overlying 45 m unconsolidated sediments which rest on a sequence of hard consolidated sediments
- Spatial variability of basal anisotropic ice and subglacial material imply different subglacial deformation mechanisms, that is, Coulomb-type of plastic deformation and a Weertman-type of sliding

Correspondence to:
C. Hofstede,
coen.hofstede@awi.de

Physical Conditions of Fast Glacier Flow: 2. Variable Extent of Anisotropic Ice and Soft Basal Sediment From Seismic Reflection Data Acquired on Store Glacier, West Greenland

C. Hofstede[1] [iD], P. Christoffersen[2] [iD], B. Hubbard[3] [iD], S. H. Doyle[3] [iD], T. J. Young[2,4] [iD], A. Diez[5] [iD], O. Eisen[1,6] [iD], and A. Hubbard[7] [iD]

[1] Alfred Wegener Institute, Helmholtz Centre for Polar and Marine Research, Bremerhaven, Germany, [2] Scott Polar Research Institute, Cambridge University, Cambridge, UK, [3] Centre for Glaciology, Department of Geography and Earth Sciences, Aberystwyth University, Aberystwyth, UK, [4] British Antarctic Survey, National Environmental Research Council, Cambridge, UK, [5] Norwegian Polar Institute, Framsenteret, Tromsø, Norway, [6] Faculty of Geosciences, University of Bremen, Bremen, Germany, [7] Centre for Arctic Gas Hydrate, Environment and Climate, Department of Geology, Arctic University of Norway, Tromsø, Norway

Abstract Outlet glaciers of the Greenland Ice Sheet transport ice from the interior to the ocean and contribute directly to sea level rise because discharge and ablation often exceed the accumulation. To develop a better understanding of these fast-flowing glaciers, we investigate the basal conditions of Store Glacier, a large outlet glacier flowing into Uummannaq Fjord in west Greenland. We use two crossing seismic profiles acquired near the centerline, 30 km upstream of the calving front, to interpret the physical nature of the ice and bed. We identify one notably englacial and two notably subglacial seismic reflections on both profiles. The englacial reflection represents a change in crystal orientation fabric, interpreted to be the Holocene-Wisconsin transition. From Amplitude-Versus-Angle (AVA) analysis we infer that the deepest ~80 m of ice of the parallel-flow profile below this reflection is anisotropic with an enhancement of simple shear of ~2. The ice is underlain by ~45 m of unconsolidated sediments, below which there is a strong reflection caused by the transition to consolidated sediments. In the across-flow profile subglacial properties vary over small scale and the polarity of the ice-bed reflection switches from positive to negative. We interpret these as patches of different basal slipperiness associated with variable amounts of water. Our results illustrate variability in basal properties, and hence ice-bed coupling, at a spatial scale of ~100 m, highlighting the need for direct observations of the bed to improve the basal boundary conditions in ice-dynamic models.

1. Introduction

Mass loss from the Greenland Ice Sheet (GrIS) consists of two main components: meltwater runoff and ice discharge into the surrounding ocean (e.g., Fürst et al., 2015). Since the late 1990s, Greenland has lost ice at an increasing rate (Bevan et al., 2012; Hanna et al., 2013; Joughin et al., 2012; Shepherd et al., 2012). The most recent estimate from 2009 to 2012 is a mass loss of 378 Gt/a equivalent to an estimated sea level rise (SLR) of 1.1 mm/a over the period 2009–2012 (Enderlin et al., 2014; Van den Broeke et al., 2016), which makes the GrIS the single largest contributor of the global cryosphere to SLR. Approximately half of this ice loss is attributed to dynamic thinning with the other half explained by surface melting and runoff (Csatho et al., 2014; Rignot & Mouginot, 2012; Van den Broeke et al., 2009). Whereas meltwater production and runoff is well represented in global sea level prediction (Intergovernmental Panel on Climate Change, 2013), the contribution to SLR resulting from ice discharge and dynamic thinning is still relatively poorly understood (e.g., Csatho et al., 2014). Several possible mechanisms have been suggested as to the cause of increased dynamic thinning. They can generally be divided into two end-members: A warmer atmosphere leading to increased surface melt which partly drains to the base, thereby enhancing sliding, or a warmer ocean interacting with the ice sheet's marine-terminating glaciers, causing melt, thereby reducing the back force and increasing outlet ice flow. Both end-members cause an increase in outlet glacier flow leading to a lowering of the ice surface resulting in an increase in the surface slope. This, in turn, increases the driving force of outlet glaciers.

An important boundary condition for ice discharge and dynamic thinning, regardless of which end-member is more important, is the nature of the subglacial material. It is especially important to establish whether ice flows over hard bedrock or water saturated sediments, and whether sliding at the bed occurs in a strict sense by deformation of ice or sediment, or a combination of both.

There is abundant evidence that fast outlet glaciers and ice streams in Antarctica are underlain by soft sediments (e.g., Alley et al., 1986; Anandakrishnan et al., 1998; Anandakrishnan, 2003; Blankenship et al., 1986; Smith & Murray, 2008; Smith et al., 2007, 2013). Thick saturated till has been identified on Antarctic ice streams giving little resistance, thus allowing fast ice flow. Routing of subglacial water is thought to be the cause of sticky spots resisting ice flow (Winberry et al., 2014), so water content in subglacial sediments regulates the basal friction and thus the sliding velocity.

It has long been thought that Greenland's outlet glaciers predominantly slide over hard bedrock. However, more recent evidence has revealed the presence of sediments beneath several areas of the GrIS (Walter et al., 2014). Christianson et al. (2014) and Vallelonga et al. (2014) recently identified dilatant till beneath the onset of the Northeast Greenland Ice Stream, demonstrating that the single largest ice stream in Greenland has soft basal conditions that are very similar to those observed more frequently beneath Antarctic ice streams. In west Greenland glacial sediments are widespread on the continental shelf (Dowdeswell et al., 2014; Hogan et al., 2012) and are also likely to be present subglacially. Dow et al. (2013) found highly porous sediments under Russell Glacier in Southwest Greenland, the same place where van de Wal et al. (2015) found seasonality in ice flow caused by water pressure build up in and release from subglacial sediments.

To identify and characterize the basal mechanical and hydrological conditions at a large, fast-flowing marine-terminating outlet glacier, we collected seismic data along two perpendicular profiles on the central flow line of Store Glacier in west Greenland.

2. Data and Methods

2.1. Field Site

Store Glacier is the third largest tidewater glacier on the west coast of Greenland (Chauché et al., 2014) with an outlet velocity of 5,300 m/a and a seasonal ice velocity variation of approximately 500–700 m/a at the terminus (Howat et al., 2010; Todd & Christoffersen, 2014). It drains an area of 35,100 km^2, has an ablation area of 5,200 km^2, and discharges approximately 12 km^3 of ice and 2–3 km^3 of meltwater in Uummannaq Fjord annually. A 450 m overdeepened trough in the fjord gives Atlantic Water access to its ice-ocean interface (Chauché et al., 2014). The seasonality of the ice flow of Store Glacier has been linked to ice-ocean interaction (Howat et al., 2010; Todd & Christoffersen, 2014). However, very little is known about basal conditions and the meltwater runoff that largely occurs subglacially.

2.2. Survey Area

The survey area is located in the ablation zone, 30 km upstream of the calving front of Store Glacier at ∼900 m elevation (Figure 1). The glacier flows here in the direction 262° relative to True North (T), at a rate of ∼600 m/a on the eastern (up-flow) side, increasing to ∼700 m/a toward the western (down-flow) side. The 2 km^2 survey area has a densely crevassed, but nevertheless accessible surface, and provides an opportunity to investigate the glacial and subglacial conditions beneath the fast-moving ice of a marine-terminating outlet glacier in an otherwise inaccessible area. Two high-resolution seismic profiles were collected in the summer of 2014. At that time the ice surface was characterized by ice, abundant drainage channels, melt ponds, moulins, and water-filled crevasses oriented perpendicular to the ice flow direction. The ice surface had some meter scale undulation, a 100 m lowering in ice flow direction (maximum surface slope of 4°), and a 30 m depression in the center of the crossline (maximum surface slope of 2°).

2.3. Seismic Data Sets

We recorded two data sets: A profiling data set to identify the substructure of the ice and subglacial material and an Amplitude-Versus-Angle (AVA) data set to identity the subsurface materials. Each data set was processed differently.

2.3.1. Profiling

We recorded two crossing seismic profiles. The first was a 2010 m along-profile, Line 1, aligned parallel to the ice flow (direction 262°); the second a 1,348 m across-profile, Line 2, aligned transverse to ice flow (direction 325°). We recorded twofold seismic data using a 300 m snow streamer consisting of 96 gimballed 30 Hz geophones (vertical P wave sensors). The shot point (SP) spacing was either 150 m or 75 m. The seismic source
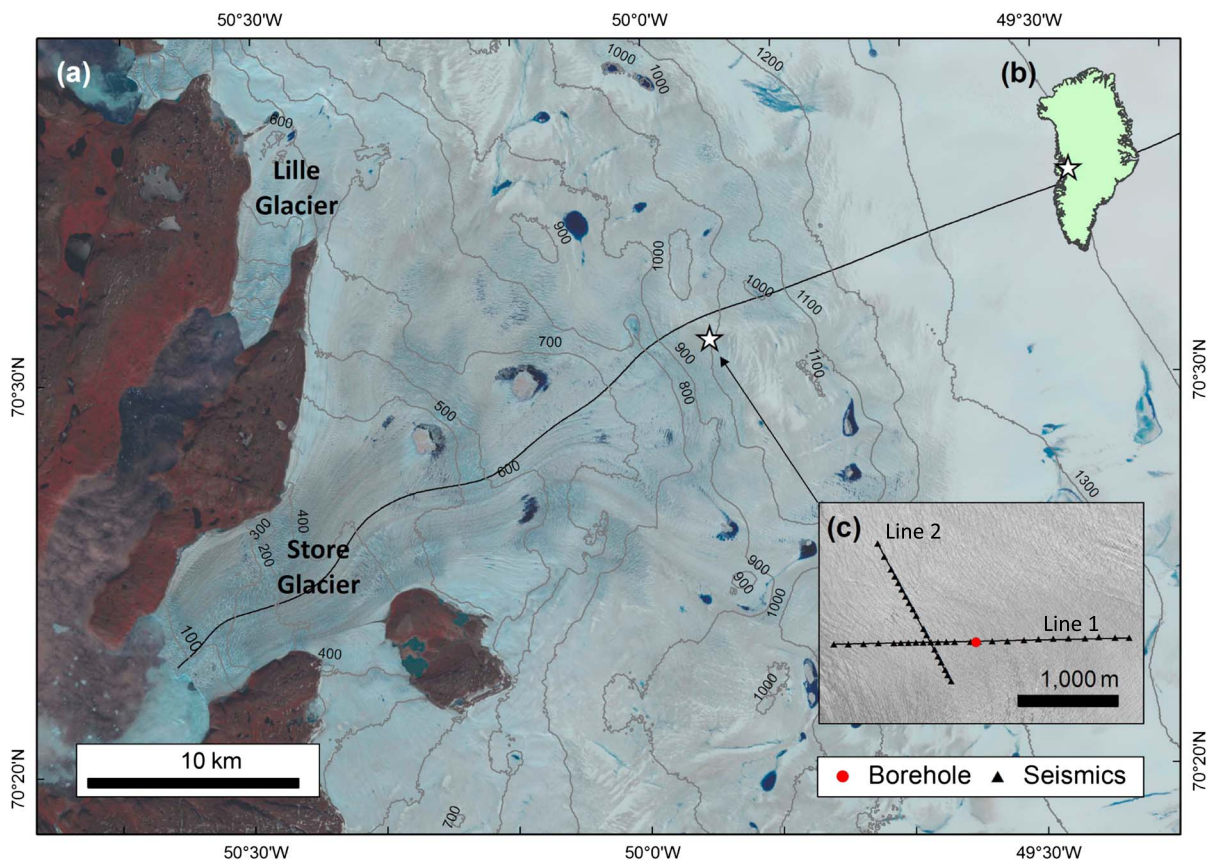
Figure 1. (a) Map from a Formosat-2 image of Store Glacier with elevation contours in meters above sea level and (b) an inset map of Greenland for its location. The star in Figure 1b marks the location of the survey area. (c) The survey area with two seismic profiles, Line 1 and Line 2, is shown in black. The black triangles represent the shot locations. The red dot represents a borehole with an installed thermistor string and tilt meters.

for each shot was a 400 g dynamite charge placed in an ~2 m deep borehole. As the surface comprised solid ice, there was no loss of elastic energy due to firn compression or diving waves. Data were recorded on four seismographs mounted on a Nansen sled that also towed the snow streamer. The streamer and sled were manually hauled across the glacier surface, but maneuverability was limited, particularly through crevassed fields. To increase the length of the seismic profiles, we recorded additional shots (SP 1 to 11), starting at 1,500 to 0 m offset, decreasing in 150 m increments, while the streamer was maintained in its initial starting position at SP 11 (Figure 2). We then moved streamer and shot together, keeping an offset of 22 m between the two
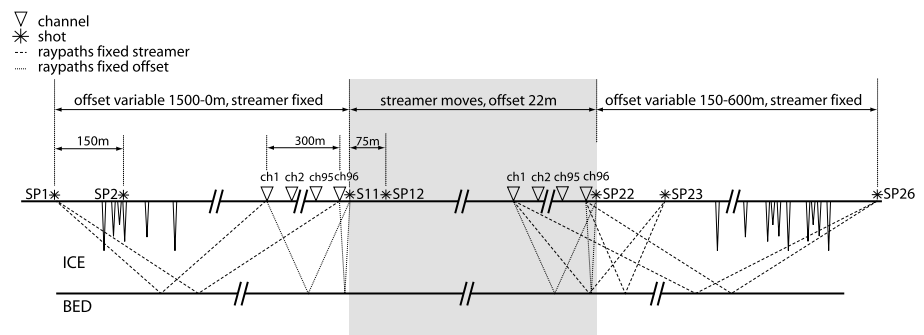

Figure 2. Diagram of the recording setup for the along-profile, Line 1. The shot interval from SP 1 to SP 11 was 150 m with a decreasing offset (1500–0 m) and keeping the streamer in starting position at SP 11. From SP 11 to SP 22 (shaded area), the shot interval was 75 m with an offset of 22 m (so the streamer moved with each shot, the common offset configuration). The streamer stayed in this end position while SP 23 to SP 26 with a shot interval of 150 m were recorded. This way the profile could be extended in more difficult terrain and remained twofold.

Table 1
Recording Geometry of Along-Profile Line 1

SP	Offset (m)	SP interval (m)	Streamer position
1–11	1,500–0	150	SP 11
12–22	22	75	SP 12–SP 22
23–26	150–600	150	SP 22

and a shot spacing of 75 m until ice surface conditions became too demanding (shaded area, SP 12 to 22). The offset operation was then repeated, maintaining the streamer in its final position and recording additional shots in steps of 150 m increasing offset (SP 23 to 26). The position of each SP was surveyed to a horizontal and vertical accuracy of 0.1 m using a Trimble R7 GPS postprocessed against correction data from Trimble NetRS base station permanently deployed on solid bedrock adjacent the glacier front. A summary is given in Table 1.

As our data were twofold processing was done in the shot domain. We processed the profiling data sets using land-based techniques but applied a few modifications caused by the specific setting (heavily crevassed ice surface). We removed noisy traces and applied manual static corrections. We used spiking deconvolution to compress the 10 ms long source wavelet and to suppress the ghost (arriving 1 to 2 ms after the primary source wavelet). We applied spatial frequency filtering (FK) to remove crevasse-generated linear moveout noise, band-pass filtering, stacking, and a poststack Kirchhoff migration. The strong vertical velocity inversions at the ice base and lateral amplitude contrast caused by highly variable attenuation of the receivers causes smiles in the migrated stacks which is why we show both the filtered stacks and migrated stacks are shown in Figure 3. We refer to these as (migrated) profiles.

2.3.2. AVA Analysis

To identify media properties above and below reflection events, we collected an AVA data set, which allows the angle of incidence dependency of a reflector to be analyzed. To preserve amplitude information as much as possible in the AVA data set, we performed two necessary processing steps: spiking deconvolution and a 10–500 Hz band-pass filter to avoid aliasing. As ghost removal was not very effective we picked the very first peak (or trough) of an event before arrival of the ghost. Reflectivity is governed by contrasts in P wave velocity (V_p), S wave velocity (V_s), density (ρ), and angle of incidence (θ), at the interface of two media (e.g., Booth et al., 2016). The only variable at a specific site is θ and as such there is a characteristic dependency of reflection coefficient R against θ. In AVA analysis this dependency is investigated and used to identify both media at the considered interface. The reflection coefficient $R(\theta)$ is quantified by Dow et al. (2013):

$$R(\theta) = \frac{A_1(\theta)}{A_0} r(\theta) e^{\alpha r(\theta)}, \tag{1}$$

where $A_1(\theta)$ is the amplitude of the primary reflection considered, A_0 the source amplitude, $r(\theta)$ the traveled distance of the primary wave, and α the attenuation. To reconstruct $R(\theta)$ of a reflector of interest, we collected the amplitude variation over a range of θ. For proper AVA analysis coverage of the same reflection area is needed. We simplified this technique by using three shots of along-profile Line 1 with an offset range from 3 to 900 m. This allowed tracking of reflectors at a continuous θ range of 0 to $\sim$ 40° covering a reflection (Common Midpoint or CMP) area of 450 m or 690 m when including the Fresnel zones (Figure 3a). By assuming the physical properties do not change over this CMP area, we can use this data set for AVA analysis. An advantage of this data set is that the streamer was fixed so that gimballed geophones could be coupled securely to the ice surface and that the coupling remained constant throughout the AVA experiment. To account for the shot to shot variability in the AVA data set, we equalized the amplitude of the top reflection at offset transitions from one shot to the next.

2.4. The Reflection Coefficient at Normal Incidence

Collecting AVA data is labor intensive and only provides local information. Considerable information in addition to the AVA data can also be obtained by analyzing the polarity of the reflection coefficient at normal incidence. The reflection coefficient at the boundary of two layered media at normal incidence is given by the acoustic impedance ($Z = \rho V_p$) on either side of the reflector:

$$R = \frac{Z_2 - Z_1}{Z_2 + Z_1} = \frac{\rho_2 V_{p_2} - \rho_1 V_{p_1}}{\rho_2 V_{p_2} + \rho_1 V_{p_1}}, \tag{2}$$
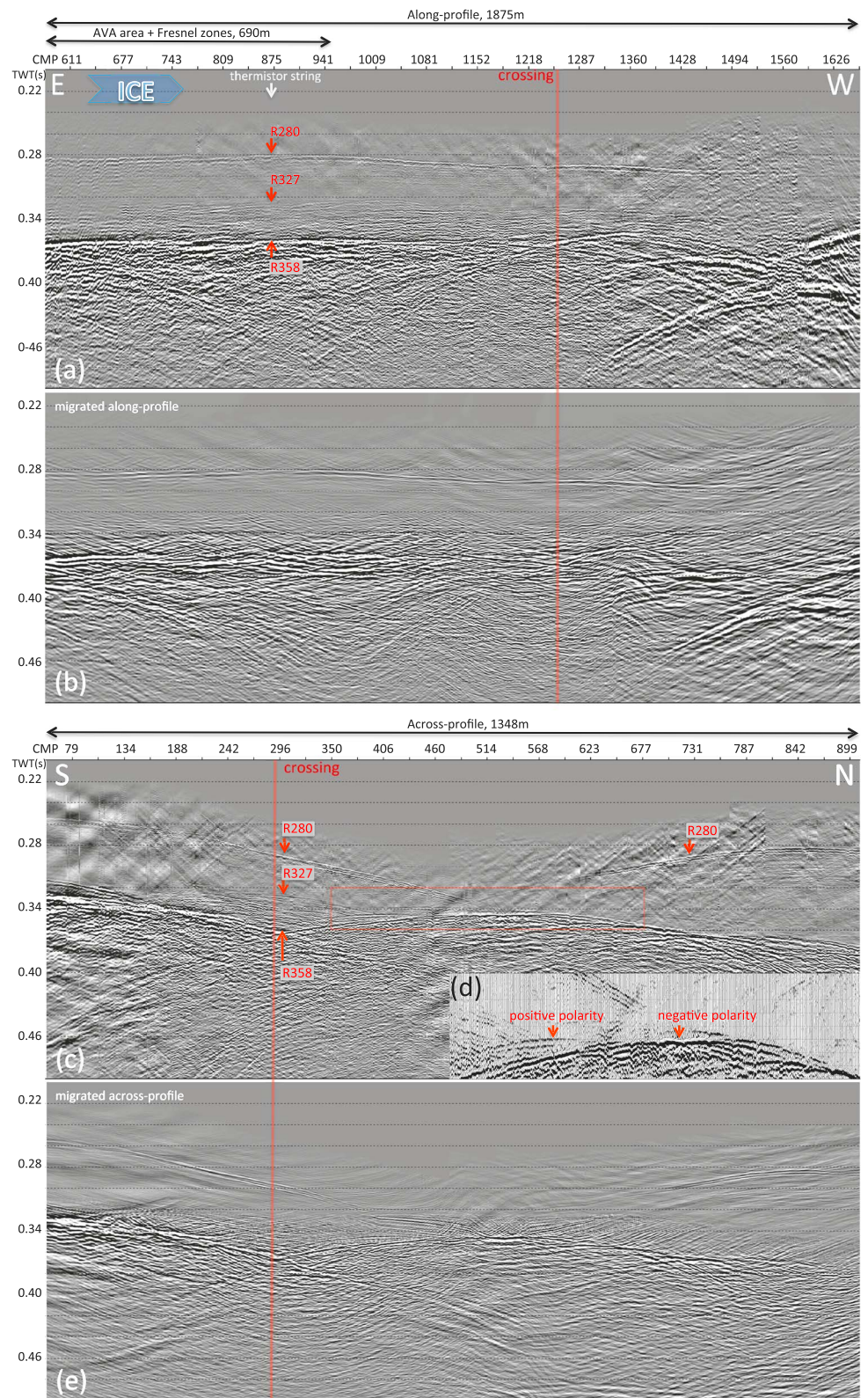
Figure 3. Seismic profiles for (a) the along-profile Line 1, (b) its migrated profile, (c) the across-profile Line 2, with an (d) inset of a polarity reversal of R358, and (e) its migrated across-profile. The three identified events R280, R327, and R358 are marked at the thermistor string location (white arrow at the top) (Figure 3a). The AVA reflection area is marked on top of Figure 3a. In Figure 3c the three events are marked, and a polarity reversal is visible in the rectangular area and inset (Figure 3d) where the englacial reflection almost attains the base.

where subscripts 1 and 2 refer to upper and lower media. The polarity of R at normal incidence is thus determined by the contrast in magnitude of the acoustic impedance Z of both media. Most of the collected profiling data were recorded with a fixed offset of 22 m making θ mostly close to normal incidence for the given ice thickness and equation (2) sufficient to represent R.

3. Results

The seismic data (Figure 3) clearly show different seismic events each with individual characteristics. The data contain various types of noise, related to the heavily crevassed surface and the summertime glacial conditions. We distinguish coherent low-frequency noise with linear moveout, noisy channels, varying frequency content in the traces caused by varying attenuation, and static variability between traces. The linear moveout noise is crevasse generated, reflecting the direct wave caused by the source as the effect is absent on noise records (i.e., recordings without a detonated shot). Noisy channels are mainly caused by poor contact of the geophones with the ice (e.g., some were occasionally hanging in crevasses) or picking up ambient noise such as running melt water. Lateral changes in attenuation are most likely caused by (water-filled) crevasses through which the source wavelet travels. This also caused varying travel times of reflections, leading to static variability between channels. Despite the high noise level several strong reflections can be clearly identified from the seismic profiles.

3.1. Identified Reflections

In both profiles we identify three important reflections, hereafter named R280, R327, and R358 after their Two Way Traveltime (TWT) relative to the starting position of the streamer (CMP 870 at the along-profile). The reflections characterize the englacial, basal, and subglacial conditions and distinguish four different media.

Reflection R280 is strongest in the central part of the along-profile from CMP 555 to CMP 1452 (Figure3a). The reflection has bed conformity and long spatial wavelength variation in the flow direction but not across-flow. The polarity of the top reflection is positive throughout the along-profile. The reflection lies at the top of an ~20 ms long series that consists of more than one reflection and fades out around CMP 1560 on the western side. At the across-profile R280 forms an almost symmetric apparent syncline or fold with a hingeline at CMP 500 (Figure 3c). In the migrated profile (Figure 3e) the hingeline cannot be tracked as it disappears in the smiles of a deeper event. The polarity and wavelet of R280 is similar on both profiles: It consists of a 20 ms long reflection series starting with small positive amplitude followed by a larger negative amplitude.

Reflection R327 is the uppermost reflection of a series of events, forming a seismically stratified sequence, approximately 30 to 40 ms long (Figure 3a). It is most clearly visible in the central part of the along-profile from CMP 685 to CMP 1297, where we recorded with a fixed offset. The reflection is discontinuous and varies in strength along-flow. The reflection fades out at the start and end of the profile where the offsets are largest (i.e., eastern side, CMP 421–CMP 685 especially between CMP 486 and CMP 583 and beyond CMP 1350 on the western side). R327 can be tracked in the across-profile but only at the crosspoint area (Figure 3c). The top of the stratification, R327, fades out on the southern side around CMP 165 and terminates sharply on the northern side at CMP 382.

Reflection R358 is the deepest notable event recorded in the along-profile and is particularly pronounced at larger offsets (Figure 3a, CMP 424–CMP 685). It appears smooth and horizontal except on the western side beyond CMP 1250 (crossing) where it has a more pronounced topography. This reflection is stronger than both R280 and R327 and mostly has a positive polarity. At larger offsets, that is, before CMP 685 and beyond CMP 1452, the resolution disappears due to increased attenuation. At smaller offsets, however, stratification is visible. At the central part of the along-profile, the reflection is not always continuous and it is difficult to discern the polarity. In the across-profile R358 shows a more pronounced topography but generally dips to the north. At the crossing at CMP 300 of the across-profile (Figures 3c and 3e), reflection R358 forms a local depression. On the southern side the polarity of reflection coefficient R is positive but on the northern side, around CMP 450, R becomes negative (Figure 3d). This part with a negative reflection coefficient (CMP 500–CMP 50) causes a strong smile in the migrated profile (Figure 3e).

Overall, the along-profile reflections are horizontal to subhorizontal and aligned parallel to each other (Figure 3a), whereas the across-profile reflections show greater roughness at the scale of ~100 m (Figures 3c and 3e).

Table 2
The RMS and Interval Velocities of Events R280, R327, and R358, Derived Using Dix's Method

Event	V_{rms} (m/s)	Depth (m)	Range V_{rms} (m/s)	Range depth z (m)	V_{int} (m/s)	Range V_{int} (m/s)
R280	3,770	528	3,718–3,830	520–536	3,770	3,718–3,830
R327	3,737	611	3,707–3,767	606–616	3,511	2,762–4,075
R358	3,660	655	3,626–3,694	649–661	1,839	1,645–3,457

Note. The interval velocities are derived for the layer above the reflection mentioned. For uncertainties see section 3.2.

3.2. Velocity Analysis and TWT Conversions

For a velocity analysis we collected an additional large offset data set (0–900 m) on the along-profile at the crosspoint (CMP 1201–CMP 1297). By using Dix's method (Dix, 1955) over a wide range of offsets, we retrieved the root-mean-square velocity (V_{rms}) and the interval velocity (V_{int}) of the media overlying the three identified reflections. The resulting V_{rms} varied within 0.5–1.5%, depending on the considered offset interval. We prescribe this variation as the uncertainty. A precondition of Dix's method is that the reflections are horizontal, which is approximately the case for the top two reflections, R280 and R327. Reflection R358 slopes $\sim$ 6° causing an overestimation of V_{rms} which we have corrected for (Dix, 1955). From V_{rms} we derived the depths z and interval velocities V_{int} for the layer above the reflections R280, R327, and R358 (Table 2). The calculated V_{int} represents the average value V_p for the whole depth interval considered between two reflections. Between 0 and 528 ± 8 m depth, $V_{int} = 3770 \pm 60$ m/s, between 528 ± 8 m and 611 ± 5 m depth, $V_{int} = 3511 \pm 750$ m/s, and between 611 ± 5 and 655 ± 6 m depth, $V_{int} = 1839 \pm 1620$ m/s.

3.3. AVA Analysis

To physically characterize the different media above and below the three different reflections, we plotted R against θ using equation (1). The AVA data consist of three shots with offset ranges from 3 to 300 m (shot 1), 303 to 600 m (shot 2), and 603 to 900 m (shot 3). To account for the shot to shot variability, we assumed a continuous transition in amplitude of reflection R280 at offset transitions from shot 1 to 2 and shot 2 to 3. This resulted in two scalars, 1.31 and 1.41, by which we multiplied the source amplitude A_0 of shots 2 and 3. The direct path method described by Holland and Anandakrishnan (2009) to determine A_0 was unsuitable as surface crevasses affected the attenuation of the direct wave too much. Offsets below 38 m were unsuitable due to source-induced noise, so the AVA data set covers an offset range from 38 to 900 m. The source-induced noise (linear moveout) partly overlaps the considered reflections, making the amplitude determination uncertain. We therefore focused the analysis on those parts without interfering noise which overly the reflections. The uncertainty of the reflection coefficient $R(\theta)$ mainly consists of two parts: uncertainty in the picked amplitude A_1 of a reflection and uncertainty in the source amplitude A_0. We approximated the uncertainty in A_1 as the mean noise level over a 5 ms time window preceding each reflection. The uncertainty of A_0 we approximated by using the multiple bounce method described by Holland and Anandakrishnan (2009) over several traces, resulting in a value of $A_0 = 1,874 \pm 330$ mV. With an attenuation $\alpha = 0.6$ km^{-1} (explained in the discussion) we calculated the reflection coefficients of the three reflections identified for angle ranges of 3–40° (Figure 4b).

The first arrivals from the uppermost reflection, R280, can be tracked from an offset of 138 to 900 m (Figure 4a). The value of R is positive, generally increasing with increasing θ (Figure 4b). Its value begins at $R = 0.01$ at $\theta = 7°$, increasing steadily to $R = 0.022$ at $\theta = 40°$.

The amplitude of R327, which is positive and small, can be tracked reasonably to an offset of 360 m; thereafter it is discontinuous (Figure 4a). The value of R varies between 0.01 and 0.03 (Figure 4b). At offsets larger than 370 m ($\theta > 17°$), the first pick is unreliable. Between offset 488 m ($\theta = 22°$) and 600 m ($\theta = 26°$) the amplitude is negative but because of the discontinuity, we cannot unambiguously assign it to R327.

Reflection R358 can be tracked from an offset of 100 to 900 m (Figure 4a). The amplitude is positive and stronger then that of R280 and R327. At closer offsets the resolution is better but the reflection is discontinuous. At larger offsets (440 to 900 m) the reflection is continuous but with less resolution. The value of R generally increases with increasing θ. It varies between 0.1 ($\theta = 4°$) and 0.2 ($\theta = 28°$), after which it decreases to 0.1 at $\theta = 33°$ (Figure 4b).
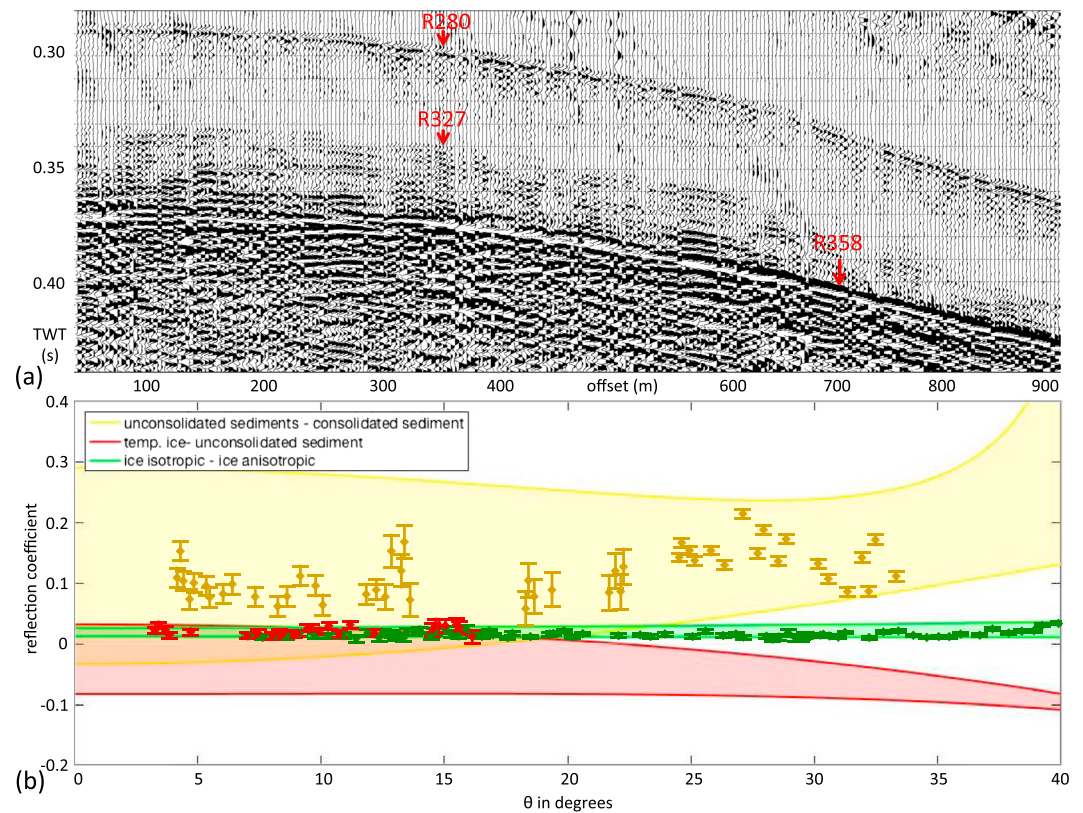
Figure 4. (a) The AVA data set with an offset range from 38 to 900 m used for the reconstruction of the reflection coefficient $R(\theta)$. (b) Calculated reflection coefficients $R(\theta)$ of the three identified reflections with error bars. Green diamonds represent englacial reflection, R280, red diamonds the top of the stratified material R327, and yellow diamonds the strongest reflection R358. The solid lines and shaded areas represent the ranges of $R(\theta)$ of different possible media contrasts encountered at the survey site.

4. Discussion

In July 2014 a thermistor string was installed at the onset of the seismic survey (i.e., CMP 870 of the along-profile) using hot-water drilling (Figure 3a). In all seven boreholes drilled in 2014 and 2016, connection to the subglacial hydrological system was confirmed by the rapid drainage of borehole water when the drill stem reached a depth of 605–611 m below the surface Doyle et al. (2018). R327 at 611 ± 5 m depth can thus accurately be interpreted to represent the ice-bed interface. Furthermore, we suggest that R280 at 528 ± 8 m depth originates from an englacial reflector and R358 at 655 ± 6 m depth is caused by the interface between the seismically stratified sequence and a hard base. From the temperature data (Figure 5) and a dominant frequency of 85 Hz we calculated the one way attenuation $\alpha = 0.6$ km^{-1} for the entire ice column (Peters et al., 2012). To identify the nature of the four media separated by the three identified reflectors and in particular the nature of the subglacial conditions, we used three analyses as follows:

The first analysis comes from the polarity of the reflection coefficient R at normal incidence given by equation (2). This condition is satisfied for the shots with a fixed 22 m offset (i.e., $1° < \theta < 16°$), which includes the majority of both profiles. Using the same values for ρ, V_p, and lithology as Christianson et al. (2014), we calculated the acoustic impedance Z (Table 3) and R at normal incidence for the most likely media contrasts (Table 4). The seismic velocities of cold and temperate ice were adjusted to the conditions of the survey area. Depending on the porosity and water saturation, the P wave velocity of temperate ice can be as low as 3,470 m/s and up to 3,740 m/s (Kim et al., 2010).

From the thermistor string data we infer that the lowest meters of the ice column are probably at the pressure melting point and thus temperate (Figure 5). Assuming we have temperate ice at the base, we interpret the values of R derived in Table 4, the polarity, and amplitude of the ice-bed reflection as follows:

1. A negative polarity indicates the presence of water; the larger the magnitude, the more water is present.
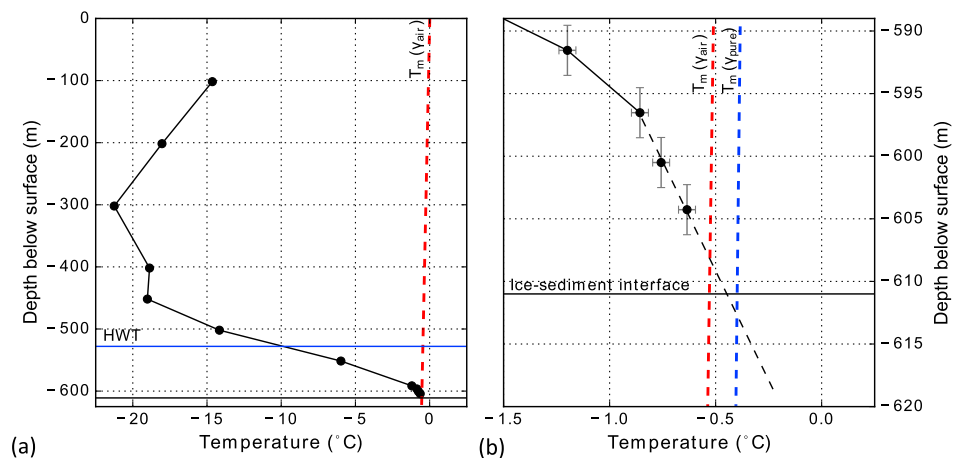
Figure 5. (a) Temperature-depth profile measured by thermistors installed in a borehole at the study site (see Figure 3a) in July 2014 and (b) a close-up near the inferred ice-sediment interface. The red and dashed subvertical blue lines are the Clausius-Clapeyron gradients for pure ice and air saturated water (Y_{air}), and pure ice and pure water (Y_{pure}), respectively. Linear extrapolation of the basal temperature gradient (black dashed line) suggests the probable existence of a thin (i.e., < 10 m) layer of temperate basal ice.

2. A positive reflection coefficient indicates a drier bed; the larger the amplitude, the larger the impedance contrast to the underlying material (a harder, denser material) generally is.
3. As the basal ice is temperate, a weak positive polarity may indicate unconsolidated sediments.

The shaded media contrast areas of $R(\theta)$ can partly overlap (Figure 4b). Distinguishing, for example, between dilatant till and unconsolidated sediments is not always possible. However, the polarity itself is a good indicator of whether water is present in the subglacial material as water tends to reduce the acoustic impedance.

The second analysis comes from the interval velocities, V_{int}, derived from the velocity analysis of the media between the three reflectors R280, R327, and R358 and the surface. As the velocity data are collected in the center of the survey area, we assume the derived velocities are representative for the whole survey area. Though the accuracy of the derived RMS velocities is only 0.5–1.5%, this accuracy causes large uncertainties in the interval velocities of the ice below the englacial reflection R280 and the stratified material. To identify the different media, we will use the most likely single interval velocity value.

The third analysis comes from the angle-dependent reflection coefficient $R(\theta)$ of the three reflectors, R280, R327, and R358.

4.1. Interpretation of the Four Media at the Interfaces of R280, R327, and R358
Migration of both the along-profile (Figure 3b) and across-profile (Figure 3e) was difficult as they suffer from smiles and a 3-D topography that is represented by 2-D profiles. We attribute the smiles to a strong velocity inversion at the ice-bed contact and to lateral variability in reflector amplitude. This amplitude variation is most likely caused by water-filled surface crevasses causing reflections of the direct wave throughout the

Table 3
Interval Velocities, Densities, and Acoustic Impedance (Z) Ranges for Glacial and Subglacial Media

Lithology	V_{int} range (m/s)	ρ range (kg/m^3)	Z range ($\times$ 1,000, kg/(m^2 s))
Cold ice	3,770–3,840	917	3,460–3,520
Temperate ice	3,470–3,740	917–921	3,180–3,440
Lithified sediments/bedrock	3,000–6,200	2,200–2,800	6,600–1,1740
Consolidated sediments	2,000–2,600	1,600–1,900	3,200–4,940
Unconsolidated sediments	1,700–1,900	1,600–1,800	2,720–3,420
Dilatant till	1,600–1,800	1,600–1,800	2,560–3,240
Water	1,450–1,500	1,000–1,020	1,450–1,600

Table 4
Ranges of R of Media Contrasts at Normal Incidence

Media contrast	R range
Cold ice-lithified sediments/bedrock	0.304 to 0.667
Cold ice-consolidated sediments	−0.047 to 0.176
Temperate ice-cons sediments	−0.003 to 0.210
Temperate ice-unconsolidated sediments	−0.084 to 0.030
Temperate ice-dilatant till	−0.114 to 0.003
Temperate ice-water	−0.379 to −0.335
Consolidated sediments-lithified sediments/bedrock	0.143 to 0.688
Unconsolidated sediments-lithified sediments/bedrock	−0.033 to 0.729

shot records but also causing different attenuation depending on the travel paths of the seismic energy. Nevertheless, we are sufficiently confident in the results of our seismic data analysis to provide the following interpretation of the observed media properties and their stratigraphy.

Reflection R280 is an englacial reflector at 528 ± 8 m depth at the thermistor string location (CMP 870 of the along-profile). It is part of a series of reflections, 20 ms long-equivalent to ~38 m of ice. The series is located at 528–566 m depth, well within the ice column and significantly above the confirmed ice-bed contact at 605–611 m depth. It is similar in appearance to the englacial reflection Horgan et al. (2008) identified at Jakobshavn Isbræ as the low-frequency arrival above which Holocene reflections appear, taking place in the lower 10–15% of the ice column. Reflection R280 appears at 14% in the lower ice column and may very well be the Holocene-Wisconsin transition which has been identified at this relative depth in this area (Karlsson et al., 2013).

R280 has a weak but positive polarity on, both the along- and across-profiles. Similar to previous seismic surveys undertaken in West Antarctica at Thwaites Glacier and Bindschadler Ice Stream (Horgan et al., 2011), the englacial reflection has bed conformity and long spatial wavelength variation in flow direction and short wavelength variation across-flow. We follow Horgan et al. (2011) in our reasoning that R280 is caused by a change in COF. Seismic *P* waves travel 5% faster parallel to the *c* axis of an ice crystal then perpendicular to it. When the ice crystals are randomly orientated, the bulk properties of ice are isotropic, but when the crystals have a preferred orientation, the bulk properties of ice become anisotropic and can, when the change in orientation is sudden, cause seismic reflections. Changes in V_p can be caused by a change in density, temperature, or crystal orientation. As R280 is within the ice column and up to ~80 m above the bed, intrusion of basal debris is unlikely and the density of ice is constant. The temperature gradient is fairly constant here (Figure 5). We hence conclude that the most likely cause of these englacial reflections is an abrupt change in COF.

Stress regimes have been identified as causes of changes in COF, most often at ice domes or divides (Alley, 1988; Budd & Jacka, 1989; DiPrinzio et al., 2005; Diez et al., 2014; Hofstede et al., 2013; Montagnat et al., 2014) but more recently also at ice streams (Christianson et al., 2014; Horgan et al., 2008, 2011). As Alley (1988) and Horgan et al. (2011) summarize, the stress regime at ice streams causes *c* axes to rotate under vertical compression and bed parallel simple shear. This rotation leads to vertical clustering of *c* axes which in its turn hardens against vertical compression but softens simple shear (Budd & Jacka, 1989)

As we identified one englacial reflection we assumed the simplest scenario, namely, that the overlying ice of R280 is isotropic even though the stress regime at the survey area is complex where we can expect converging and stretching ice flow and consequently anisotropic overlying ice (Harland et al., 2013). The values of $R(\theta)$ fall within the green shaded area (Figure 4b), which represents the theoretical transition from isotropic ice to a Vertical Transverse Isotropic (VTI) structure with a cone opening angle of 0 (upper limit) to 45° (lower limit). Reflection R280 most likely marks the transition from isotropic to a (almost) VTI structure with a cone opening angle up to 45°. This anisotropic ice is vertically less compressible but horizontally twice more easily deformable, having an enhancement factor of ~2 for simple shear (Cuffey & Paterson, 2010; Thorsteinsson, 2000). The value of the enhancement factor may be affected by the assumption of overlying isotropic ice.

The interval velocity of the top 528 ± 8 m of ice is $3,770 \pm 60$ m/s (Table 2). While this is slow for cold isotropic ice, the velocity is likely reduced by the presence of liquid water held within the ice matrix and crevasses.

The interval velocity of the anisotropic ice below R280 is $3,511 \pm 750$ m/s (Table 2). We assume the entire ice column below R280 is anisotropic because there are no deeper reflections that show otherwise and because VTI structures found in ice cores in Greenland are present over longer depth ranges whereby the cone angle θ typically increases with increasing depth (Gow et al., 1991; Gusmeroli et al., 2012; Thorsteinsson et al., 1999).

We interpret R327 as the ice-bed contact at 611 ± 5 m depth at the thermistor string location. It is the top of a 45 m thick stratified sequence extending to R358 at 655 ± 6 m depth with an interval velocity of $1,839 \pm 1,620$ m/s. Considering the interval velocity of $1,839 \pm 1,620$ m/s and the weakness of R327 that occasionally disappears in the central part of the along-profile (22 m offset, $1° < \theta < 16°$), we interpret the subglacial material as unconsolidated sediments. This interpretation was supported in 2016, when the hot-water drilling team was able to penetrate, haltingly and over some hours, some tens of meters into this sequence (Doyle et al., 2018). The reflection coefficient $R(\theta)$ (Figure 4b) can be tracked from an angle of 4 to 16° where it has a positive but weak polarity. The till can be interpreted as an unconsolidated sediment having a positive reflection coefficient if overlain by temperate ice or if water is distributed widely in the pores of the sediment throughout the sequence. The disappearance of R327 at the start and end of the along-profile we attribute to a $\theta \geqslant 16°$ and thus a decreasing $R(\theta)$, a characteristic of a temperate ice-unconsolidated sediment interface.

Reflector R358 has a positive polarity throughout the along-profile. It is notably stronger than R327 and R280. The reflection coefficient $R(\theta)$ is positive throughout the angle interval from 0 to 40° (Figure 4b) with a value of $R(\theta) = 0.1$ at 4° to $R(\theta) = 0.2$ at 28°. The values fall well within the $R(\theta)$ interval of an unconsolidated-consolidated sediment interface (yellow shaded area) and are interpreted as such. This interpretation is confirmed by the increasing trend of $R(\theta)$ with increasing θ that is a characteristic of an unconsolidated-consolidated sediment interface. The reflection coefficient has a maximum around 28°, which seems unusual as the theoretically derived graph has a maximum at 40°, but this maximum is formed by the largest possible contrast of V_p, V_s, and ρ. It is more likely that the contrast of V_p, V_s, and ρ are less than the maximum contrast, as the stratified material between R327 and R358 is more consolidated with depth and probably have increasing values for V_p, V_s, and ρ with increasing depth.

4.2. Glaciological Implications of COF and Unconsolidated Basal Sediment

From the structure of the three events discussed in the results and the identification of the four media of the seismic profiles (Figure 3), we now discuss the glaciological implications.

In the along-profile we identified 80 m of anisotropic ice below R280 and $\sim$45 m of unconsolidated till below R327, both of which are more easily deformable than the upper 530 m of cold, stiff, isotropic ice and have important implications for ice flow. Doyle et al. (Doyle et al., 2018) reported that at CMP 870, $63-71\%$ of the observed surface velocity of 592 m/a takes place as basal sliding or as deformation in the subglacial sediments and that the remaining $29-37\%$ is explained by ice deformation which predominantly occurs in the lowermost 80 m of the ice column. Based on the current understanding of subglacial tills, we consider a Coulomb plastic rheology to be the most likely (Bougamont et al., 2014; Clarke et al., 2005), suggesting that the subglacial deformation will likely be concentrated at its top near the ice base and not distributed over the depth of the basal till layer. The observed increased consolidation with depth in the till layer is most likely an attribute of the till layer's own overburden pressure. While the effective pressure at the base is likely to be very small, a hydrostatic equilibrium would mean that effective pressure increases linearly with depth according to the difference between till density and the density of water contained in its pores

At the across-profile R280 forms an apparent syncline or fold. If R280 is the Holocene-Wisconsin transition as our data suggest, it would be an isochrone. The consequence is that at the deepest point of the syncline at CMP 500, that is, the older anisotropic ice, has disappeared. We hypothesize that the apparent syncline formed because ice flow in the drainage basin generally converges and that basal melting has caused the anisotropic ice to be lost. At the same time the unconsolidated till clearly terminates in the northerly direction at CMP 382 in the across-profile beyond which R358 becomes the ice-bed contact. This means that at the syncline's hinge point, reflection R358 is the ice-bed contact. We interpret its negative polarity to be caused by the presence of a large amount of subglacial water, which most likely is exclusively present at the ice-bed interface because ice at this location is in direct contact with the consolidated (R358) sediment observed below the till layer when the latter is present. We therefore conclude that ice must be sliding over a bed consisting of consolidated sediments at the syncline's hinge point at CMP 500.

Both profiles display different characteristics in bed stratigraphy. The along-profile (Figures 3a and 3b) shows less spatial variation and a more consistent top to bottom stratigraphy, whereas the across-profile (Figures 3c–3e) shows greater spatial variability in both the presence of anisotropic ice and the subglacial deposits. Considering the patchy character of the ice-bed contact in the across-profile, we can expect different types of ice and sediment deformation in different areas.

In order to quantify the deformation of subglacial till the along-profile would require a flow law for subglacial sediments, for example, a Coulomb-type plastic flow. For parts of the across-profile, where our analysis indicates the presence of consolidated sediments and subglacial water, a more traditional Weertman-type flow law would seem equally appropriate. The subglacial water content most likely varies over time and influences both a Coulomb type of till deformation and Weertman sliding, so preferably both flow laws should be able to take time-varying subglacial water pressures into account.

Ryser et al. (2014) observed and modeled the complex ice dynamics in along-flow direction caused by subglacial patches with varying basal slipperiness over time and space. Overlying colder and stiffer ice would enhance horizontal stress transfer between patches. They concluded that the ice dynamics in the ablation area was a result of an integrated response to the locally and time-varying ice-bed conditions. Our results reveal subglacial patches of different basal slipperiness of similar dimensions, overlain by colder stiffer ice. We infer that the distribution of subglacial water varies spatially with water partly present in the unconsolidated till layer and partly present in a basal water system at the ice-bed interface and almost certainly variable over time as the bed of Store Glacier accommodates a large amount of surface water during summer.

Our observations indicate that realistic modeling of ice dynamics in this region can be based on either a Coulomb-type plastic flow for till or a Weertman-type sliding law or equivalent. The advantage of the former is that basal traction can evolve from changes in the storage of water in the till layer (Bougamont et al., 2014). The advantage of the latter is that basal traction can evolve according to the configuration of a basal water system, which can be either be distributed or channelized. At the moment it is difficult to tell which model offers the best advantage, given that both till and basal water systems are likely to exert direct influence on ice flow.

5. Conclusions

In two profiles, parallel and transverse to the ice flow, we identified three seismic events separating four different media within and beneath Store Glacier. From the derived interval velocities and the reflection coefficients we interpreted the four different media to be (1) an upper ∼530 m thick layer of isotropic ice; (2) an ∼80 m thick layer of anisotropic ice, most likely having a VTI structure; (3) an ∼45 m thick layer of unconsolidated and acoustically stratified till; and (4) a harder base consisting of consolidated sediments.

These three seismic events could be tracked throughout both profiles but with changing stratigraphy and structure. The along-profile contains subhorizontal reflectors with little topography and little spatial variation, whereas the across-profile has considerable topography and spatial variation. The across-profile contains dipping englacial reflections and an absence of the oldest anisotropic ice at the hinge of the syncline-like structural fold. We hypothesize that the syncline formed in response to converging ice flow and that the oldest ice at the bottom of the hinge lines axial plane was lost due to basal melting. We also found a phase shift from positive to negative polarity which we interpret as a change from water stored preferential in the pore spaces of a relatively thick subglacial till layer to water contained largely at the ice-bed interface where till is absent and ice is underlain by a consolidated and more compact sediment. These observations suggest that we can expect two different types of ice and sediment deformation within less than a kilometer of each other: a Coulomb type of plastic flow where the unconsolidated till below the ice is present and a Weertman type of sliding where consolidated sediments and subglacial water are present. We do not know whether free water at the basal interface requires till to be absent as found here, or whether the latter is a coincidence. We conclude by stating that these type of bed properties and their spatial variations seem to be common in Western Greenland (e.g., Ryser et al., 2014). But direct observations from the bed are of advantage to decide for the optimal basal parameterization in numerical ice flow models and whether those should include till as well as basal water systems.

Our observations imply that realistic modeling of ice dynamics in this region require a combination of both a Coulomb-type plastic flow for till and a Weertman-type sliding law or equivalent. How such a hybrid

parameterization could be implemented under transient subglacial drainage and ice flow dynamics at typical higher-order ice sheet model grid resolutions (1–10 km) remains a major outstanding challenge for accurate forecasting of Greenland's fast-flowing outlet glaciers.

References

Alley, R. B. (1988). Fabrics in polar ice sheets: Development and prediction. *Science*, *240*(4851), 493–495. https://doi.org/10.1126/science.240.4851.493

Alley, R. B., Blankenship, D. D., Bentley, C. R., & Rooney, S. T. (1986). Deformation of till beneath ice stream B, West Antarctica. *Nature*, *322*(6074), 57–59. https://doi.org/10.1038/322057a0

Anandakrishnan, S. (2003). Dilatant till layer near the onset of streaming flow of Ice Stream C, West Antarctica, determined by AVO (amplitude vs offset) analysis. *Annals of Glaciology*, *36*, 283–286. https://doi.org/10.3189/172756403781816329

Anandakrishnan, S., Blankenship, D., Alley, R., & Stoffa, P. (1998). Influence of subglacial geology on the position of a West Antarctic ice stream from seismic observations. *Nature*, *394*, 62–65. https://doi.org/10.1038/27889

Bevan, S., Luckman, A., & Murray, T. (2012). Glacier dynamics over the last quarter of a century at Helheim, Kangerdlugssuaq and 14 other major Greenland outlet glaciers. *The Cryosphere*, *6*, 923–937. https://doi.org/10.5194/tc-6-923-2012

Blankenship, D. D., Bentley, C. R., Rooney, S. T., & Alley, R. B. (1986). Seismic measurements reveal a saturated porous layer beneath an active Antarctic ice stream. *Nature*, *322*(6074), 54–57. https://doi.org/10.1038/322054a0

Booth, A. D., Emir, E., & Diez, A. (2016). Approximations to seismic AVA responses: Validity and potential in glaciological applications. *Geophysics*, *81*(1), 1–11. https://doi.org/10.1190/GEO2015-0187.1

Bougamont, M., Christoffersen, P., Hubbard, A., Fitzpatrick, A., Doyle, S. H., & Carter, S. P. (2014). Sensitive response of the Greenland Ice Sheet to surface melt drainage over a soft bed. *Nature Communications*, *5*, 5052. https://doi.org/10.1038/ncomms6052

Budd, W. F., & Jacka, T. H. (1989). A review of ice rheology for ice sheet modelling. *Cold Regions Science and Technology*, *16*, 107–144. https://doi.org/10.1016/0165-232X(89)90014-1

Chauché, N., Hubbard, A., Gascard, J.-C., Box, J. E., Bates, R., Koppes, M., . . . Patton, H. (2014). Ice-ocean interaction and calving front morphology at two west Greenland tidewater outlet glaciers. *The Cryosphere*, *8*, 1457–1468. https://doi.org/10.5194/tc-8-1457-2014

Christianson, K., Peters, L. E., Alley, R. B., Anandakrishnan, S., Jacobel, R. W., Riverman, K. L., . . . Keisling, B. A. (2014). Dilatant till facilitates ice-stream flow in northeast Greenland. *Earth and Planetary Science Letters*, *401*, 57–69. https://doi.org/10.1016/j.epsl.2014.05.060

Clarke, G. K. C., L'homme, N., & Marshall, S. J. (2005). Tracer transport in the Greenland ice sheet: Three-dimensional isotopic stratigraphy. *Quaternary Science Reviews*, *24*(1–2), 155–171. https://doi.org/10.1016/j.quascirev.2004.08.021

Csatho, B., Schenk, A., van der Veen, C., Babonis, G., Duncan, K., Rezvanbehbahani, S., . . . van Angelen, J. (2014). Laser altimetry reveals complex pattern of Greenland Ice Sheet dynamics. *Proceedings of the National Academy of Sciences*, *111*, 18,478–18,483. https://doi.org/10.1073/pnas

Cuffey, K., & Paterson, W. (2010). *The physics of glaciers, fourth edition* (4th ed.). Burlington: Elsevier. https://doi.org/10.3189/002214311798843412

Diez, A., Eisen, O., Weikusat, I., Eichler, J., Hofstede, C., Bohleber, P., . . . Polom, U. (2014). Influence of ice crystal anisotropy on seismic velocity analysis. *Annals of Glaciology*, *55*(67), 97–106. https://doi.org/10.3189/2014AoG67A002

DiPrinzio, C. L., Wilen, L. A., Alley, R. B., Fitzpatrick, J. J., Spencer, M. K., & Gow, A. J. (2005). Fabric and texture at Siple Dome, Antarctica. *Journal of Glaciology*, *51*(171), 281–290. https://doi.org/10.3189/172756505781829359

Dix, C. (1955). Seismic velocities from surface measurements. *Geophysics*, *20*(1), 68–86. https://doi.org/10.1190/1.1438126

Dow, C., Hubbard, A., Booth, A., Doyle, S., Gusmeroli, A., & Kulessa, B. (2013). Seismic evidence of mechanically weak sediments underlying Russell Glacier, West Greenland. *Annals of Glaciology*, *54*, 135–141. https://doi.org/10.3189/2013AoG64A032

Doyle, S. H., Hubbard, B., Christoffersen, P., Young, T. J., Hofstede, C., Bougamont, M., . . . Hubbard, A. (2018). Physical conditions of fast glacier flow: 1. Measurements from boreholes drilled to the bed of Store Glacier, West Greenland. *Journal of Geophysical Research: Earth Surface*, *123*. https://doi.org/10.1002/2017JF004529

Dowdeswell, J., Hogan, K., Cofaigh, C., Fugelli, E., Evans, J., & Noormets, R. (2014). Late Quaternary ice flow in a West Greenland fjord and cross-shelf trough system: Submarine landforms from Rink Isbrae to Uummannaq shelf and slope. *Quaternary Science Reviews*, *92*, 292–309. https://doi.org/10.1016/j.quascirev.2013.09.007

Enderlin, E., Howat, I., Jeong, S., Noh, M. J., van Angelen, J., & Van den Broeke, M. (2014). An improved mass budget for the Greenland ice sheet. *Geophysical Research Letters*, *41*, 866–871. https://doi.org/10.1002/2013GL059010

Fürst, J., Goelzer, H., & Huybrechts, P. (2015). Ice-dynamic projections of the Greenland Ice Sheet in response to atmospheric and oceanic warming. *The Cryosphere*, *9*, 1039–1062. https://doi.org/10.5194/tc-9-1039-2015

Gow, A. J., Meese, D. A., Alley, R. B., Fitzpatrick, J. J., Anandakrishnan, S., Woods, G. A., & Elder, B. C. (1991). Physical and structural properties of the Greenland Ice Sheet project 2 ice cores: A review. *Journal of Geophysical Research*, *102*(C12), 26,583–26,599. https://doi.org/10.1029/97JC00165

Gusmeroli, A., Pettit, E. C., Kennedy, J. H., & Ritz, C. (2012). The crystal fabric of ice from full-waveform borehole sonic logging. *Journal of Geophysical Research*, *117*, F03021. https://doi.org/10.1029/2012JF002343

Hanna, E., Navarro, F., Pattyn, F., Domingues, C., Fettweis, X., Ivins, E., . . . Zwally, J. (2013). Ice-sheet mass balance and climate change. *Nature*, *498*, 51–59. https://doi.org/10.1038/nature12238

Harland, S. R., Kendall, J. M., Stuart, G., Lloyd, G. E., Baird, A. F., Smith, A., . . . Brisbourne, A. M. (2013). Deformation in Rutford Ice Stream, West Antarctica: Measuring shear-wave anisotropy from icequakes. *Annals of Glaciology*, *54*, 105–114. https://doi.org/10.3189/2013AoG64A033

Hofstede, C., Eisen, O., Jansen, D., Kristoffersen, Y., Lambrecht, A., & Mayer, C. (2013). Investigating englacial reflections with vibro- and explosive-seismics surveys at Halvfarryggen ice dome, Antarctica. *Annals of Glaciology*, *54*(64), 189–200. https://doi.org/10.3189/2013AoG64A064

Hogan, K., Dowdeswell, J., & Cofaigh, C. (2012). Glacimarine sedimentary processes and depositional environments in an embayment fed by West Greenland ice streams. *Marine Geology*, *311*, 1–16. https://doi.org/10.1016/j.margeo.2012.04.006

Holland, C., & Anandakrishnan, S. (2009). Subglacial seismic reflection strategies when source amplitude and medium attenuation are poorly known. *Journal of Glaciology*, *55*, 931–937. https://doi.org/10.3189/002214309790152528

Horgan, H., Anandakrishnan, S., Alley, R. B., Burkett, P. G., & Peters, L. (2011). Englacial seismic reflectivity: Imaging crystal-orientation fabric in West Antarctica. *Journal of Glaciology*, *57*(204), 639–650. https://doi.org/10.3189/002214311797409686

Horgan, H. J., Anandakrishnan, S., Alley, R. B., Peters, L. E., Tsoflias, G. P., Voigt, D. E., & Winberry, J. P. (2008). Complex fabric development revealed by englacial seismic reflectivity: Jakobshavn Isbræ, Greenland. *Geophysical Research Letters*, *35*, L10501. https://doi.org/10.1029/2008GL033712

Howat, I. M., Box, J. E., Yushin, A., Herrington, A., & McFadden, E. M. (2010). Seasonal variability in the dynamics of marine-terminating outlet glaciers in Greenland. *Journal of Glaciology*, *56*(198), 601–613. https://doi.org/10.3189/002214310793146232

Intergovernmental Panel on Climate Change (2013). *Climate change 2013: The physical science basis. Contribution of Working Group I to the IPCC Fifth Assessment Report of the Intergovernmental Panel on Climate Change*. In T. F. Stocker, et al. (Eds.), (Vol. AR5). Cambridge UK and New York: Cambridge University Press.

Joughin, I., Alley, R. B., & Holland, D. (2012). Ice-sheet response to oceanic forcing. *Science*, *338*, 1172–1176. https://doi.org/10.1126/science.1226481

Karlsson, N. B., Dahl-Jensen, D., Gogineni, S. P., & Paden, J. (2013). Tracing the depth of the Holocene ice in North Greenland from radio-echo sounding data. *Annals of Glaciology*, *54*(64), 44–50. https://doi.org/10.3189/2013AoG64A057

Kim, K. Y., Lee, J., Hong, M. H., Hong, J. K., Jin, Y. K., & Shon, H. (2010). Seismic and radar investigations of Fourcade Glacier on King George Island, Antarctica. *Polar Research*, *29*, 298–310. https://doi.org/10.1111/j.1751-8369.2010.00174.x

Montagnat, M., Azuma, N., Dahl-Jensen, D., Eichler, J., Fujita, S., Gillet-Chaulet, F., … Weikusat, I. (2014). Fabric along the NEEM ice core, Greenland, and its comparison with GRIP and NGRIP ice cores. *The Cryosphere*, *8*, 1129–1138. https://doi.org/10.5194/tc-8-1129-2014

Peters, L. E., Anandakrishnan, S., Alley, R. B., & Voigt, D. E. (2012). Seismic attenuation in glacial ice: A proxy for englacial temperature. *Journal of Geophysical Research*, *117*, F02008. https://doi.org/10.1029/2011JF002201

Rignot, E., & Mouginot, J. (2012). Ice flow in Greenland for the International Polar Year 2008–2009. *Geophysical Research Letters*, *39*, L11501. https://doi.org/10.1029/2012GL051634

Ryser, C., Luethi, M., Andrews, L., Catania, G., Funk, M., Hawley, R., … Neumann, T. (2014). Caterpillar-like ice motion in the ablation zone of the Greenland ice sheet. *Journal of Geophysical Research: Earth Surface*, *119*, 2258–2271. https://doi.org/10.1002/2013JF003067

Shepherd, A., Ivins, E., Geruo, A., Barletta, V., Bentley, M., Bettadpur, S., … Zwally, H. (2012). A reconciled estimate of ice-sheet mass balance. *Science*, *338*, 1183–1189. https://doi.org/10.1126/science.1228102

Smith, A., & Murray, T. (2008). Bedform topography and basal conditions beneath a fast-flowing West Antarctic ice stream. *Quaternary Science Reviews*, *28*, 584–596. https://doi.org/10.1016/j.quascirev.2008.05.010

Smith, A., Murray, T., Nicholls, K., Makinson, K., Adalgeirsdottir, G., Behar, A., & Vaughan, D. (2007). Rapid erosion, drumlin formation, and changing hydrology beneath an Antarctic ice stream. *Geology*, *35*(2), 127–130. https://doi.org/10.1130/G23036A.1

Smith, A., Jordan, T., Ferraccioli, F., & Bingham, R. (2013). Influence of subglacial conditions on ice stream dynamics: Seismic and potential field data from Pine Island Glacier, West Antarctica. *Journal of Geophysical Research: Solid Earth*, *118*, 1471–1482. https://doi.org/10.1029/2012JB009582

Thorsteinsson, T. (2000). Anisotropy of ice Ih: Development of fabric and effects of anisotropy on deformation (PhD thesis). University of Washington.

Thorsteinsson, T., Waddington, E. D., Taylor, K. C., Alley, R. B., & Blankenship, D. D. (1999). Strain-rate enhancement at dye 3, Greenland. *Journal of Glaciology*, *45*(150), 338–345. https://doi.org/10.1017/S0022143000001830

Todd, J., & Christoffersen, P. (2014). Are seasonal calving dynamics forced by buttressing from ice mélange or undercutting by melting? Outcomes from full-Stokes simulations of Store Glacier, West Greenland. *The Cryosphere*, *8*, 2353–2363. https://doi.org/10.5194/tc-8-2353-2014

Vallelonga, P., Christianson, K., Alley, R. B., Anandakrishnan, S., Christian, J. E. M., Dahl-Jensen, D., … Winstrup, M. (2014). Initial results from geophysical surveys and shallow coring of the Northeast Greenland Ice Stream (NEGIS). *The Cryosphere*, *8*, 1275–1287. https://doi.org/10.5194/tc-8-1275-2014

van de Wal, R. S. W., Smeets, C. J. P. P., Boot, W., Stoffelen, M., van Kampen, R., Doyle, S. H., … Hubbard, A. L. (2015). Self-regulation of ice flow varies across the ablation area in south-west Greenland. *The Cryosphere*, *9*, 603–611. https://doi.org/10.5194/tc-9-603-2015

Van den Broeke, M., Bamber, J., Ettema, J., Rignot, E., Schrama, E., van de Berg, W. J., … Wouters, B. (2009). Partitioning recent Greenland mass loss. *Science*, *326*, 984–986. https://doi.org/10.1126/science.1178176

Van den Broeke, M., Enderlin, E., Howat, I., Munneke, P. K., Noël, B., van de Berg, W. J., … Wouters, B. (2016). On the recent contribution of the Greenland ice sheet to sea level change. *The Cryosphere*, *10*, 1933–1946. https://doi.org/10.5194/tc-10-1933-2016

Walter, F., Chaput, J., & Luethi, M. (2014). Thick sediments beneath Greenland's ablation zone and their potential role in future ice sheet dynamics. *Geology*, *42*, 487–490. https://doi.org/10.1130/G35492.1

Winberry, J. P., Anandakrishnan, S., Alley, R. B., Douglas, A. W., & Pratt, M. J. (2014). Tidal pacing, skipped slips and the slowdown of Whillans Ice Stream, Antarctica. *Journal of Hydrometeorology*, *60*(222), 795–807. https://doi.org/10.3189/2014JoG14J038